Lawrence Berkeley National Laboratory

Title

Failure Process During Fast Charging of Lithium Metal Batteries with Weakly Solvating Fluoroether Electrolytes

Permalink

https://escholarship.org/uc/item/3zd030hf

Authors

Chen, Yuelang

Yu, Zhiao

Gong, Huaxin

et al.

Publication Date

DOI

Copyright Information

THE JOURNAL OF PHYSICAL CHEMISTRY C
A JOURNAL OF THE AMERICAN CHEMICAL SOCIETY

Article

Failure Process During Fast Charging of Lithium Metal Batteries with Weakly Solvating Fluoroether Electrolytes

Published as part of The Journal of Physical Chemistry C virtual special issue "Jens K. Nørskov Festschrift".

Yuelang Chen, Zhiao Yu, Huaxin Gong, Wenbo Zhang, Paul Rudnicki, Zhuojun Huang, Weilai Yu, Sang Cheol Kim, David T. Boyle, Philaphon Sayavong, Hasan Celik, Rong Xu, Yangju Lin, Shaoyang Wang, Jian Qin, Yi Cui,* and Zhenan Bao*

Cite This: https://doi.org/10.1021/acs.jpcc.4c01740

Read Online

ACCESS | Metrics & More | Article Recommendations | Supporting Information

ABSTRACT: While improving the lithium metal (Li) Coulombic efficiency has been a focus for electrolyte design, the performance under high current densities is less studied yet highly relevant for practical applications. Here, we evaluate the charge-rate-dependent cycling stability using three types of weakly solvating fluoroether electrolytes. Although good cycle life was achieved in all three electrolytes under low current densities, they all exhibited a soft shorting behavior above various threshold current densities (between 2 and 5.2 mA cm^{-2}). We attributed the current-dependent electrode morphology to both Li growth and residual solid electrolyte interface (rSEI) growth processes. In early cycles, Li morphology guided the formation of rSEI structures. In later cycles, the rSEI structure partially impacted Li growth. Under low current densities, the rSEI was inhomogeneous with large voids for subsequent bulky lithium growth. Under high current densities, the rSEI became more dense, which aggravated the high-surface/volume-ratio Li growth through and on the top of the rSEI. Among the three weakly solvating fluoroether electrolytes, the ones with lower ionic conductivity were observed to short within fewer cycles and at lower charge current densities. Our work suggests that fast ion transport in electrolytes may be a desirable feature for the stable operation at >1C charging in high-energy-density lithium metal batteries.
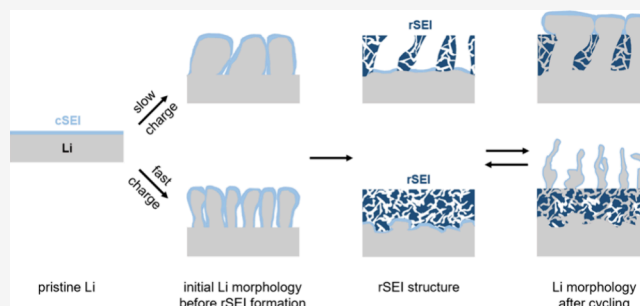
INTRODUCTION

As the world transitions toward renewable energy, there is an increasing demand for high-energy-density batteries beyond lithium-ion batteries (LIBs). The most ambitious negative electrode chemistry is pure lithium metal (Li), which provides more than 10 times the theoretical specific capacity compared to graphite. Despite great progress toward improving the Coulombic efficiency (CE) of the Li electrode,[1−19] its rate performance (particularly charge rate) is less explored. In comparison, fast charging at 4C or above has been proposed for LIBs for electric vehicles (EVs).[20] Therefore, for lithium metal batteries (LMBs) to become competitive with the incumbent, fast charging deserves further research.

Earlier investigations on carbonate electrolytes in LMBs[21] concluded that the poor cycle life under high charging current densities was due to the thick and resistive degradation layer formed on the Li surface, instead of short circuit by the Li filament growth.[22,23] More recently, the field has seen many new electrolytes with greatly improved cycling stability. However, most of these electrolytes were tested with charging current densities lower than 1 mA cm^{-2} (Supplementary Figure S1 and notes, with details in Table S1). Therefore, it is crucial to evaluate the cycling stability and understand the failure mechanisms under higher current densities.

Herein, we investigate the fast-charging behavior of LMBs using three types of weakly solvating fluoroether electrolytes: 1 M lithium bis(fluorosulfonyl)imide (LiFSI) in 1:3 (v/v) 1,2-diethoxyethane: 2,2,3,3-tetrafluoro-1,4-diethoxylbutane (DEE-FDEB), 1.54 M LiFSI in 1:3.6 (v/v) 1,2-dimethoxyethane: 1,1,2,2-tetrafluoroethyl-2,2,3,3-tetrafluoropropyl ether (DME-TTE),[3,6] and 1 M LiFSI in 2,2,3,3-tetrafluoro-1,4-dimethoxylbutane (FDMB)[2] (Figure 1a). The concentrations for DME-TTE and FDMB were determined according to the previous literature reports.[2,3] DEE-FDEB has not been reported previously. The standard concentration of 1 M LiFSI was used for DEE-FDEB, and the 1:3 (v/v) ratio of DEE:FDEB was optimized. These electrolytes were selected for their high
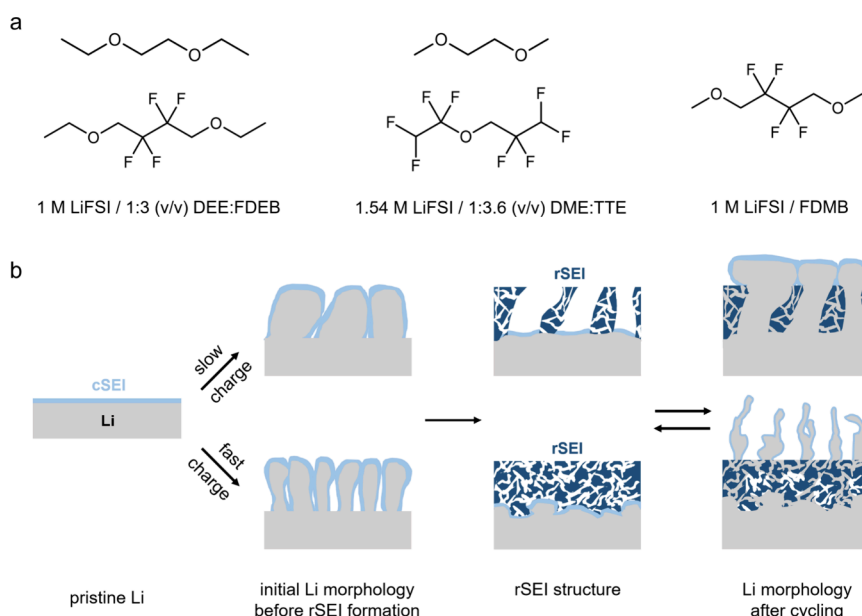
Figure 1. (a) Chemical structures and compositions of the weakly solvating fluoroether electrolytes studied in this work. (b) Overview of the current-dependent Li and rSEI growth processes proposed in this work. The compact solid electrolyte interface (cSEI) refers to the passivation layer on the Li surface. The residual solid electrolyte interface (rSEI) refers to the layer of decomposition products that do not passivate Li.

CE at low current densities (>99% by the modified Aurbach method[24]), good oxidation stability, and different ionic conductivities. By systematically varying the charge rates, we observed a short circuit in all three electrolytes above a certain current density (5.2 mA cm^{-2} for the DEE-FDEB electrolyte, 2 mA cm^{-2} for DME-TTE and FDMB electrolytes). We attributed the poor fast-charging stability to the current-dependent Li deposition morphology and residual solid electrolyte interface (rSEI) structure (Figure 1b). We observed that the initial Li growth morphology guided the formation of the rSEI structure, which then greatly impacted the subsequent Li plating morphology. The rSEI formed under a low current density (0.4 mA cm^{-2}) was inhomogeneous with large voids as a result of bulky Li growth. In contrast, the rSEI formed under a high current density (4 mA cm^{-2}) was more compact, which could aggravate the high-surface/volume-ratio Li growth through and on top of the rSEI. Among the three fluoroether electrolytes, the ones with lower ionic conductivity were observed to short within fewer cycles and at lower charge current densities. Therefore, this study suggests that fast Li$^+$ ion transport through the electrolyte may be a desirable feature for the stable operation of LMBs under high charging current densities.

METHODS

Materials. LiFSI was purchased from Arkema. DME (anhydrous, 99.5%), ethyl p-toluenesulfonate (98%), and iodomethane (99%) were purchased from Sigma. DEE (99%) was purchased from Fisher. 2,2,3,3-Tetrafluoro-1,4-butanediol (97%) and TTE (99%) were purchased from Synquest. Sodium hydride (60% in paraffin) was purchased from TCI. Celgard 2325 (25 μm thick, polypropylene/polyethylene/polypropylene) was purchased from Celgard. Cu foil (25 μm thick) was purchased from Alfa Aesar. Thick Li (600−750 μm thick) and thin Li foils (50 μm thick, free-standing) were purchased from China Energy Lithium and MSE Supplies. Single-sided NMC811 positive electrode sheets (ca. 4.5 mAh cm^{-2}) were purchased from Targray. All of the other components for 2032-type coin cells were purchased from MTI.

Synthesis and Purification. FDMB was synthesized as described previously.[2] For FDEB (Supplementary Figure S35), a solution of 2,2,3,3-tetrafluoro-1,4-butanediol (1 equiv) in THF was cooled in an ice bath, to which sodium hydride (2.5 equiv, 60% in paraffin) was added slowly under vigorous stirring. After H$_2$ bubbling stopped, ethyl p-toluenesulfonate (2.2 eqv.) was added in one portion, and the reaction mixture was stirred at room temperature for 3 h, followed by heating at 60 °C overnight. The reaction mixture was filtered, and THF was removed by a rotary evaporator. The crude product was purified by vacuum distillation three times, with the second and third times over sodium hydride to remove water. The purity of the FDEB product was confirmed by NMR (Supplementary Figures S36−S38). DEE and TTE were purified once by vacuum distillation over sodium hydride. All solvents were stored in an argon glovebox with fresh Li to remove trace amounts of water.

Electrochemical Measurements. All coin cells were fabricated as the 2032 type, with Celgard 2325 as the separator. Electrochemical measurements were carried out on Arbin, Land, and Biologic systems.

Full cells were assembled with NMC811 (ca. 4.5 mAh cm^{-2}), 50 μm Li foil (N/P ∼ 2), and 40 μL of electrolyte (E/C ∼ 8.9 mL Ah^{-1}). The cells were cycled between 2.8 and 4.4 V versus Li$^+$/Li. Two formation cycles at 0.4 mA cm^{-2} charge and discharge current densities were performed, followed by long-term cycling at various charge current densities (from 0.4 to 5.2 mA cm^{-2}) and 4 mA cm^{-2} discharge current density. A constant voltage step was applied at the end of charging until the current fell below 0.4 mA cm^{-2}.

Positive electrode half-cells were assembled in the same way as full cells except for using thick Li as the negative electrode. The cycling protocol was the same as full cells at 4 mA cm^{-2} charge and discharge current densities. The positive electrode of each cell after about 40−50 cycles was used to construct a

new positive electrode half-cell to continue the cycling. Additional positive electrode half-cells were also assembled with 80 μL of electrolyte (E/C ~ 17.8 mL Ah^{1-}).

Li negative electrode (50 μm Li) half-cells were assembled with thick Li as the counter electrode and 40 μL of electrolyte. Two formation cycles at 0.4 mA cm^{-2} were followed by long-term cycling at 4 mA cm^{-2} for 4 mAh cm^{-2} in each step. Chronopotentiometry was also carried out using Li negative electrode half-cells. The cells were precycled twice at 0.4 mA cm^{-2} for 4 mAh cm^{-2}. Then, a constant current of 4 mA cm^{-2} was applied until cell shorting. Alternatively, two cycles at 0.4 mA cm^{-2} for 4 mAh cm^{-2} and 30 cycles at 4 mA cm^{-2} for 4 mAh cm^{-2} were applied before a constant current of 4 mA cm^{-2} was applied until cell shorting. In addition, the changes in bulk resistance and interfacial resistance of Li negative electrode half-cells were tracked during cycling. The cells were activated for two cycles at 0.4 mA cm^{-2} for 4 mAh cm^{-2}. Then, the EIS measurement was carried out every 10 cycles at 4 or 0.4 mA cm^{-2} for 4 mAh cm^{-2}. The resistance values were obtained from curve fitting of Nyquist plots using the equivalent circuit (R1 + Q2/R2 + Q3/R3 + W1), where R1 is the bulk resistance and (R2 + R3) is the interfacial resistance.

Li||Cu half-cells were assembled with thick Li, Cu foil, and 40 μL of electrolyte. CE was measured by a modified Aurbach method. The Cu surface was preconditioned by plating 5 mAh cm^{-2} of Li and completely stripping to 1 V. A reservoir of 5 mAh cm^{-2} of Li was plated, followed by plating and stripping 1 mAh cm^{-2} of Li for 10 cycles and then stripping to 1 V. The current density was 0.5 mA cm^{-2} for all steps. The CE was calculated as the ratio between the total amount of Li stripped and that plated. In addition, cyclic voltammetry was performed at 1 mV s^{-1} between −0.1 and 1.5 V versus Li$^+$/Li, starting with a cathodic scan.

Li||Al cells were assembled with thick Li, 40 μL of electrolyte, Al foil (2.11 cm^2), and Al-clad positive electrode cases. The oxidative stability of each electrolyte was evaluated by linear scanning voltammetry from an open-circuit voltage to 5.5 V versus Li$^+$/Li at 1 mV s^{-1}, followed by 5.5 V hold for about 18 h. In addition, cyclic voltammetry was performed at 1 mV s^{-1} between 0.1 V versus OCV and 4.5 V versus Li$^+$/Li, starting with an anodic scan.

Li||Pt cells were assembled with thick Li, 40 μL of electrolyte, and Pt-clad positive electrode cases. Cyclic voltammetry was performed at 1 mV s^{-1} between 0.1 V versus OCV and 4.5 V versus Li$^+$/Li, starting with an anodic scan.

The intrinsic ionic conductivity was measured in a Swagelok-type cell with symmetric stainless-steel electrodes and without a separator. The apparent ionic conductivity in a cell was measured by stainless-steel symmetric coin cells with an electrolyte-soaked separator.

Solvation energy measurement was described previously.[25] The homemade apparatus was composed of a T-shaped glass flange assembled between an H-cell. Each of the three chambers contained a test electrolyte, a reference electrolyte, or a salt bridge electrolyte. Two porous junctions, each made of four layers of Celgard 2325, separated the three chambers. Two pieces of fresh lithium foil were used as the electrodes. Biologic VMP3 was used to measure the cell potential. Voltage was recorded after stabilization, which typically took up to 3 min.

The Li$^+$ transport number was measured in Li||Li symmetric cells by the Vincent–Bruce method. The interface was stabilized by five cycles at 0.5 mA cm^{-2} for 1 mAh cm^{-2}. Chronoamperometry was carried out at 10 mV for 1 h, with EIS before and after polarization.

The effective Fickian diffusivity (D_{eff}) of LiFSI in the electrolyte-soaked Celgard 2325 separator was measured by the restricted diffusion method.[26−28] The Li||Li symmetric cells were constructed using 50 μm thick Li foil (5/8 in. diameter) and 10 pieces of the Celgard 2325 separator (each 25 μm thick). The concentration gradient was established by applying a potentiostatic hold for 10 min, followed by measuring the decay of the open-circuit voltage (OCV). The potentiostatic hold voltage was selected such that the initial OCV decay started around 50 mV, ensuring an approximately linear relationship between the OCV and concentration polarization. The effective Fickian diffusivity in the separator was calculated based on

$$\lim_{t \to \infty} \frac{d \ln(OCV)}{dt} = -\frac{\pi^2 D_{eff}}{L^2}$$

where t is time, and L is the interelectrode distance (250 μm). For each electrolyte, the measurement was carried out at three different potentiostatic hold voltages, validating that the calculated D_{eff} is irrespective of the initial concentration gradient. The results were averaged.

The exchange current density for interfacial charge transfer was calculated as discussed previously.[29] Full details of the measurement can be found in that reference. A beaker cell with about 1 mL of electrolyte, a lithium counter electrode (Alfa Aesar), and a home-built tungsten disc ultramicroelectrode (radius = 12.5 μm) was used. Previously, a third Li$_4$Ti$_5$O$_{12}$ reference electrode was used. However, a two-electrode cell was also sufficient, given the low nominal currents. The iR drop was measured by EIS prior to the cyclic voltammetry measurement for compensation. The resistance was generally about 4−10 kΩ. Scan rates of 100−200 V s^{-1} were used for the CV measurements.[29] The low overpotential data in the reverse sweep were used to calculate the exchange current density via $j = j_0 f(E − E_{eq})$, where $f = F/RT$.

Galvanostatic staircase measurement of Li electrodeposition was described in detail previously.[30] A three-electrode and iR-corrected beaker cell was used. The working electrode was a homemade 0.005 cm^2 Cu electrode, and the counter and reference electrodes were made of Li metal. The Cu electrode was brought from its open-circuit voltage (~3 V vs Li$^+$/Li) to 10 mV at −50 μA cm^{-2} to reduce residual CuO and form an SEI layer on Cu. After the voltage reached 10 mV versus Li$^+$/Li, a constant current of 0.5 mA cm^{-2} was applied until the capacity reached 0.1 mAh cm^{-2}. Then, the cell was rested for 15 min. The current was then increased from 0.1 to 10 mA cm^{-2} at 120 s intervals.

Material Characterizations. One-dimensional NMR spectra were collected on a Varian Inova 500 MHz spectrometer at 25 °C. A coaxial insert containing 1 M LiCl in D$_2$O was used as the external standard for a 0 ppm shift.

DOSY NMR samples were prepared in an argon glovebox by using a coaxial insert setup. Benzene-d$_6$ was placed in the inner tube for lock and shim. In the outer tube, anhydrous toluene (0.1 vol equiv) was added into the electrolytes as an internal standard for viscosity change. The samples in Supplementary Figure S3c were measured on a 500 MHz Bruker Avance I spectrometer following the same procedure as described in detail previously.[12] The calculation of coordination percen-
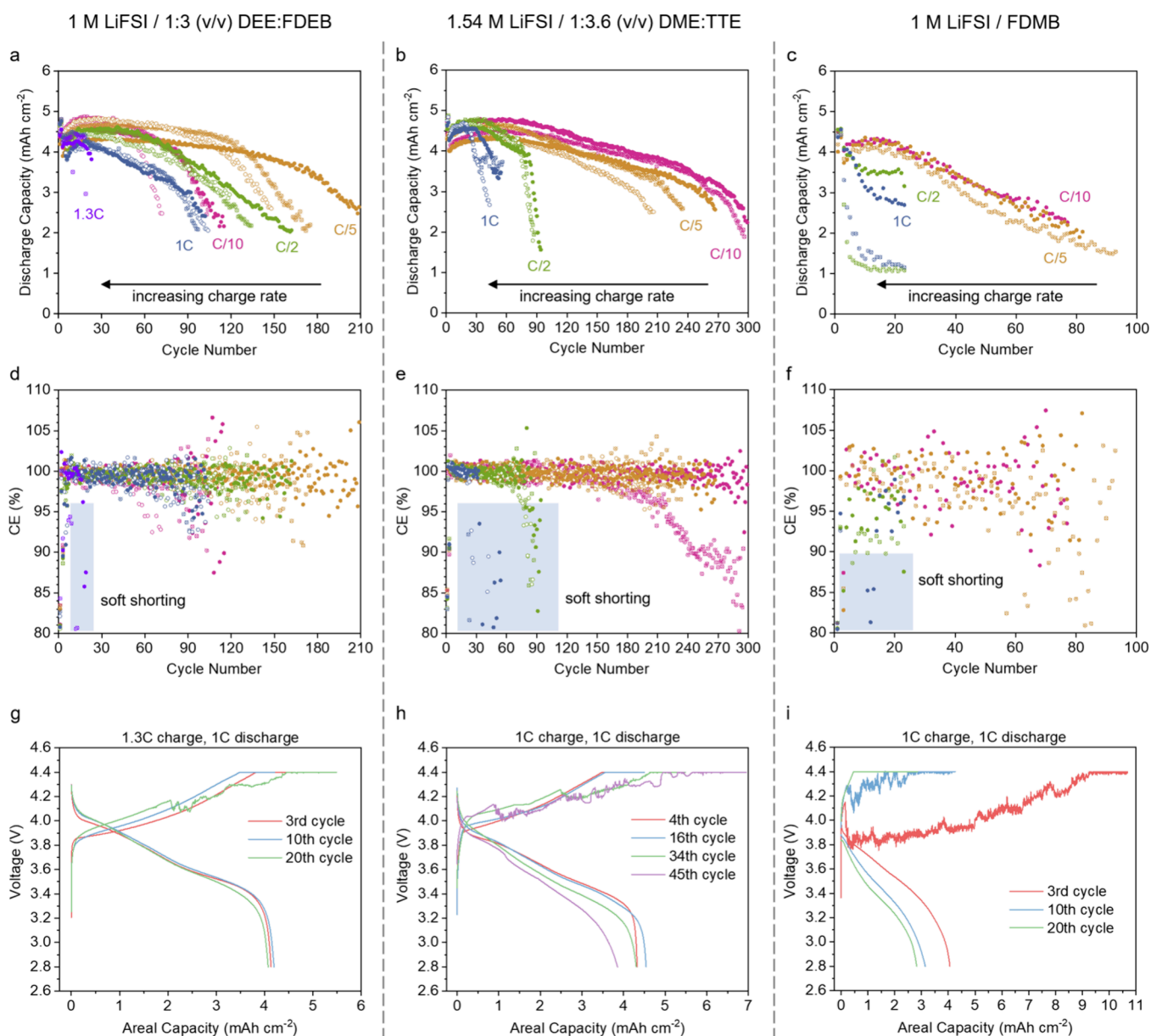
Figure 2. Full-cell performance at various charge rates and 1C discharge rate (1C = 4 mA cm^{-2}). The coin cells were assembled with NMC811 (ca. 4.5 mAh cm^{-2}), 50 μm thick Li foil (N/P $\sim$ 2), and relatively lean electrolyte amount (E/C $\sim$ 8.9 mL Ah^{-1}). All cells were cycled between 2.8 and 4.4 V versus Li$^+$/Li. Two formation cycles at C/10 charge and discharge rates were performed, followed by long-term cycling at various charge rates (labeled on the graph) and a 1C discharge rate. A constant voltage step was applied at the end of charging until the current fell below C/10. (a−c) Discharge capacity and (d−f) CE over cycling for (a−d) DEE-FDEB, (b−e) DME-TTE, and (c−f) FDMB electrolytes. The replicated cells are shown with the same color and different symbols. See Supplementary Figure S39 and notes for data reproducibility. (g,i) Voltage profiles showing soft shorting characteristics at 1.3C charge rate in DEE-FDEB (g) and 1C charge rate in DME-TTE (h) and FDMB (i).

tages was described earlier.[31] The samples, as shown in Figure 3b, were measured on a 400 MHz Varian NMR spectrometer at 25 °C. ^{7}Li- and ^{19}F-pulsed field gradient (PFG) measurements were performed to determine the self-diffusion coefficients of Li$^+$ and FSI$^-$ using dbppste_cc and pgste pulse sequences, respectively. An array of gradient strength was set to 2.908−12.504 G cm^{-1} with 12 linear steps. Appropriate diffusion delay (Δ) and gradient pulse duration (δ) were selected to ensure a sufficient signal decay. Self-diffusion coefficients were calculated by fitting peak integrals to the Stejskal−Tanner equation.

Raman spectra were collected on a Horiba XploRA+ confocal Raman with a 532 nm excitation laser. The electrolytes were sealed under argon in quartz cuvettes.

The surface morphology of Al and Li was imaged by an FEI Magellan 400 XHR SEM instrument with EDS capability. The residual salt on the electrodes was rinsed off with the corresponding solvents. The Al electrodes were obtained from the Li‖Al cells after 5.5 V holding, as shown in Supplementary Figure S6. To obtain the Li electrodes, Li negative electrode half-cells were assembled as described above. The cells were precycled twice at 0.4 mA cm^{-2} for 4 mAh cm^{-2}, followed by 10 cycles of either 4 mA cm^{-2} plating and striping (high-current formation) or 0.4 mA cm^{-2} plating

281 and 4 mA cm^{-2} stripping (low-current formation) for 4 mAh
282 cm^{-2} to form the rSEI. In the final step, 0.2, 0.5, or 1 mAh
283 cm^{-2} capacity was plated at 4 mA cm^{-2} (high-current plating)
284 or 0.4 mA cm^{-2} (low-current plating) current densities. SEM
285 imaging was carried out using 5 kV and 100 pA. For some
286 samples, elemental mapping was carried out by EDS to confirm
287 the regions of SEI and Li metal. A lower voltage of 2 kV was
288 used to minimize the interaction volume of the electrons.

289   The cross section of the rSEI was imaged by an FEI Helios
290 NanoLab 600i DualBeam SEM/FIB with EDS capability. Li‖
291 Cu half-cells were assembled as described above. The Cu
292 electrode surface was preconditioned by 10 cycles between 0
293 and 1 V at 0.2 mA cm^{-2}, followed by plating for 4 mAh cm^{-2}
294 and stripping to 1 V at 0.4 mA cm^{-2} for two cycles. Then,
295 either 10 or 30 cycles were carried out with 4 mAh cm^{-2} Li
296 plating and stripping to 1 V. The plating current density was
297 either 0.4 mA cm^{-2} (low current) or 4 mA cm^{-2} (high
298 current), and the stripping current density was 4 mA cm^{-2} for
299 all samples. The cells were disassembled in the stripped state.
300 Pt was deposited on the top surface to protect the surface
301 structure. Cross sections were prepared by Ga$^+$ ion beam. For
302 some samples, elemental mapping was carried out by EDS to
303 confirm the regions of the rSEI.

304   **MD Simulation.** Molecular dynamics simulations were
305 carried out using GROMACS 2018,[32] with electrolyte molar
306 ratios taken from those used in the experimental work.
307 Molecular forces were calculated using the optimized
308 potentials for liquid simulations all atom (OPLS-AA) force
309 field.[33] Topology files and bonded and Lennard−Jones
310 parameters were generated using the LigParGen server.[34]
311 Atomic partial charges were calculated by fitting the molecular
312 ESP at atomic centers in Gaussian16 using the Møller−Plesset
313 second-order perturbation method with a cc-pVTZ basis set.[35]
314 Due to the use of a nonpolarizable force field, partial charges
315 for charged ions were scaled by 0.8 to account for electronic
316 screening, which has been shown to improve the predictions of
317 interionic interactions.[36,37] The simulation procedure consisted
318 of energy minimization using the steepest descent method,
319 followed by 8 ns equilibration step using a Berendsen barostat
320 and a 40 ns production run using a Parrinello−Rahman
321 barostat, both at a reference pressure of 1 bar with a timestep
322 of 2 fs. A Nose−Hoover thermostat was used throughout with
323 a reference temperature of 300 K. The particle mesh Ewald
324 method was used to calculate electrostatic interactions with a
325 real space cutoff of 1.2 nm and a Fourier spacing of 0.12 nm.
326 The Verlet cutoff scheme was used to generate pairlists. A
327 cutoff of 1.2 nm was used for nonbonded Lennard−Jones
328 interactions. Periodic boundary conditions were applied in all
329 directions. Bonds with hydrogen atoms were constrained.
330 Convergence of the system energy, temperature, and box size
331 were checked to verify equilibration. The final 30 ns of the
332 production run was used for the analysis.

333   Density profiles and RDFs were generated by using
334 GROMACS. Solvation shell statistics were calculated using
335 the MDAnalysis Python package[38] by histogramming the
336 observed first solvation shells for lithium ions during the
337 production simulation, using a method similar to that of
338 previous work.[2] The cutoff distance for each species in the first
339 solvation shell was calculated from the first minimum
340 occurring in the RDF (referenced to lithium ions) after the
341 initial peak.

RESULTS AND DISCUSSION

342 Three types of weakly solvating fluoroether electrolytes (Figure
343 1a) were selected for this study since they have been identified
344 as a promising class of electrolytes for LMBs. All of them
345 exhibited good stability at the high-voltage positive electrode
346 and Li metal negative electrode, while the ion transport
347 properties vary.[2,3,6] DME-TTE and FDMB showed relatively
348 low ionic conductivities, while DEE-FDEB was formulated as a
349 more conductive weakly solvating fluoroether electrolyte.
350 Detailed characterizations and discussions on the new DEE-
351 FDEB electrolyte are provided in Supporting Information
352 Figures S2−S8 and notes. The electrochemical stability of
353 these electrolytes on Cu, Al, and Pt was probed by cyclic
354 voltammetry (Supplementary X-ray Figure S40).

355   **Charge-Rate-Dependent Full-Cell Cycle Life.** To
356 observe the effects of the charge rate on the full-cell cycle
357 life, we constructed coin cells mimicking the conditions in a
358 high-energy-density battery. A high-loading NMC811 positive
359 electrode (ca. 4.5 mAh cm^{-2}) was paired with a thin Li foil (50
360 μm thick, negative/positive capacity ratio N/P ∼ 2) and with a
361 relatively lean electrolyte amount (electrolyte/capacity ratio E/
362 C ∼ 8.9 mL Ah^{1-}). Previous studies on ether and carbonate
363 electrolytes found that Li metal cycling stability was improved
364 by setting the discharge rate higher than the charge rate.[39−41]
365 To avoid this complication, we set the discharge rate to 1C
366 (1C = 4 mA cm^{-2}) for all cells, and we selected slower or equal
367 charge rates up to 1C (except for 1.3C for the better-
368 performing DEE-FDEB). In addition, since the cycle life of
369 LMBs is sensitive to cycling capacity, we applied a constant
370 voltage charging step at the upper cutoff voltage (4.4 V) with a
371 C/10 current cutoff to ensure similar initial cycling capacity
372 regardless of the charge rates.

373   The discharge capacity and CE at various charge rates for
374 each electrolyte are listed in Figure 2a−f. For all three
375 electrolytes, the full-cell cycle life decreased as the charging
376 rate increased. The only exception was DEE-FDEB cells at C/
377 10, which showed worse performance than those at faster rates.
378 This might be due to the accumulated parasitic reactions at a
379 longer cycling time.[42]

381   A threshold charge rate was observed for each electrolyte,
382 above which cells consistently failed by soft shorting (1.3C for
383 DEE-FDEB electrolyte, C/2 for DME-TTE electrolyte, and C/
384 2 for FDMB electrolyte), as evidenced by a sharp decrease in
385 CE (Figure 2d−f shaded region and Figure S9) and spiky
386 voltage curves during charging (Figures 2g−i and S10). Here,
387 the soft shorting refers to the repeated destruction and
388 reformation of Li filament shorts, which led to the observed
389 unstable voltage at high charge rates. Similar observations have
390 previously been reported, and it was hypothesized that the thin
391 filaments may act as fuse which burns out when a large current
392 is passed through.[43,44] During the subsequent fast discharge, a
393 normal voltage curve was observed (Figures 2g−i and S10)
394 likely due to dynamic polarization[45] and/or electrochemical
395 dissolution of Li filaments.

396   If the cells were cycled continuously after soft shorting, they
397 would eventually become completely shorted. We carried out
398 additional full-cell cycling at 1C charge and discharge rates to
399 facilitate visual inspection after cell failure. The cell with the
400 DEE-FDEB electrolyte did not show soft shorting at 1C or any
401 sign of Li penetration through the separator after 82 cycles
402 (Figure S11a and notes). The DME-TTE cell endured 80
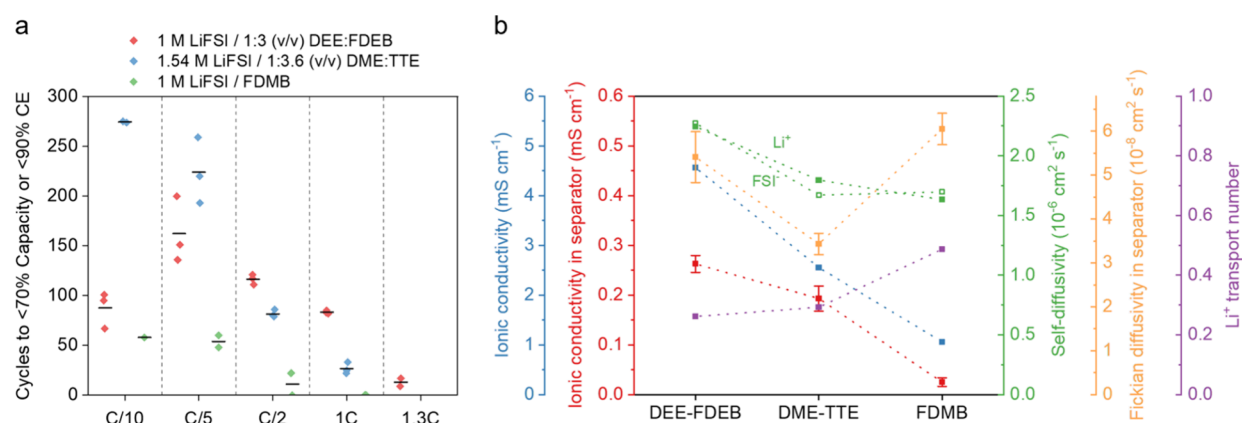403 cycles until complete short circuit, and we observed large areas

Figure 3. (a) Charge-rate-dependent full-cell cycle life. The cycle numbers were calculated from the cells, as shown in Figure 2. The end of cycle life was defined as <70% discharge capacity of the third cycle or <90% CE starting from the fourth cycle. The black lines indicate the averages. See Supporting Information Figure S39 and notes for data reproducibility. (b) Transport properties of the fluoroether electrolytes: ionic conductivity (blue), ionic conductivity in Celgard 2325 (red, average of three measurements each), self-diffusivity (green) of Li^+ (filled symbols) and FSI^- (hollow symbols), Fickian diffusivity of salt in electrolyte-soaked Celgard 2325 (orange, details in Supplementary Figure S41), and Li^+ transport number measured by Vincent−Bruce method (purple). Note: self-diffusivity and Fickian diffusivity describe diffusion without and with concentration gradient, respectively.
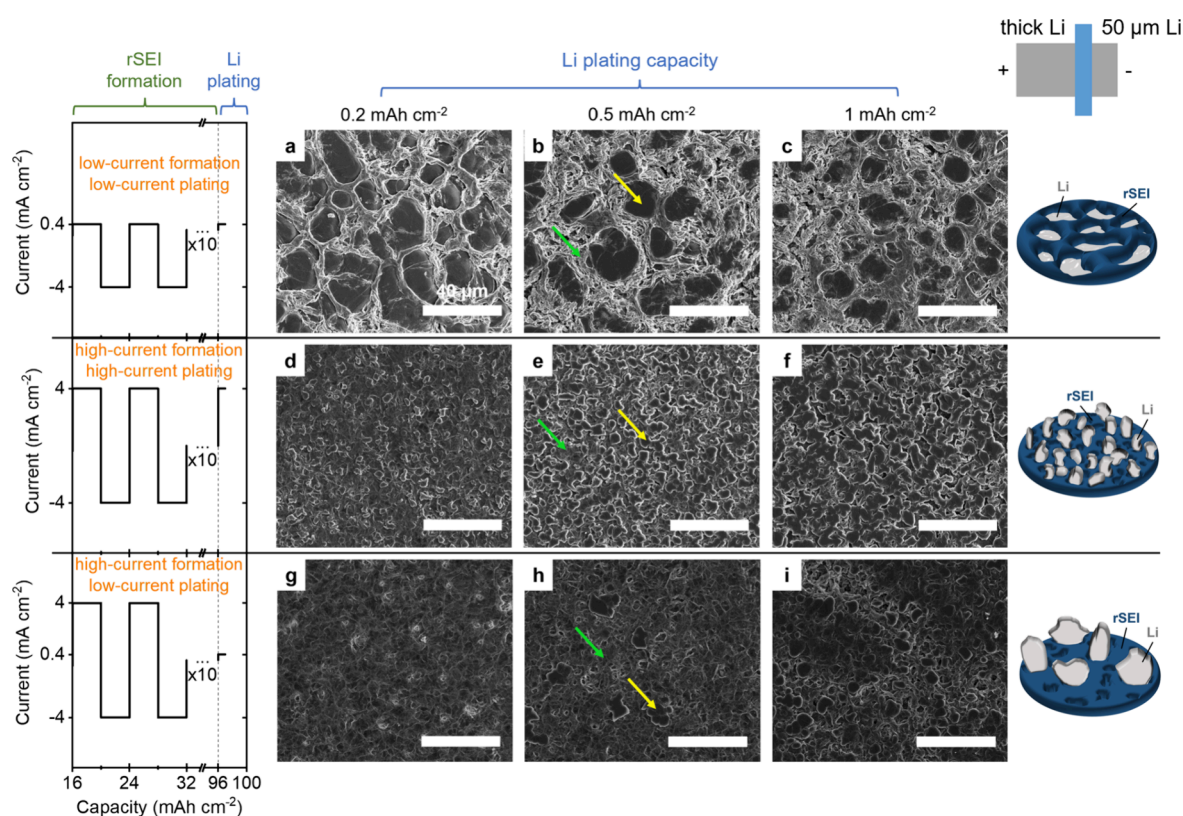

Figure 4. Secondary electron SEM images of Li plating morphology on a 50 μm Li electrode at various current densities and areal capacities in DEE-FDEB electrolyte. The rSEI was formed by 10 cycles at either 4 mA cm^{-2} plating and striping (high-current formation) or 0.4 mA cm^{-2} plating and 4 mA cm^{-2} stripping (low-current formation) for 4 mAh cm^{-2}. In the final step, 0.2, 0.5, or 1 mAh cm^{-2} capacity was plated at 4 mA cm^{-2} (high-current plating) or 0.4 mA cm^{-2} (low-current plating). The applied current profiles for rSEI formation and final Li plating are shown on the left (with complete profiles in Figure S12), where the positive current corresponds to Li plating on the 50 μm Li negative electrode (consistent with full cells). The capacities of the final Li plating are labeled by columns on the top. Yellow and green arrows indicate Li and the rSEI, respectively. The scale bars are 40 μm. The schematics on the right illustrate the top surface morphologies of Li and rSEI.

of the separator penetrated by Li filaments (Supplementary Figure S11b and notes). Interestingly, the FDMB cell showed soft shorting mostly in the early cycles, followed by a low cycling capacity in the later cycles. We were unable to see any Li filament in the separator after 62 cycles, likely due to its reversibility or small quantity of filament formation (Figure S11c and notes).

At higher charge rates ($\geq$C/2), we observed a casual correlation between cycling stability and ionic conductivity (σ) (Figure 3). For example, at 1C charge, no soft shorting was
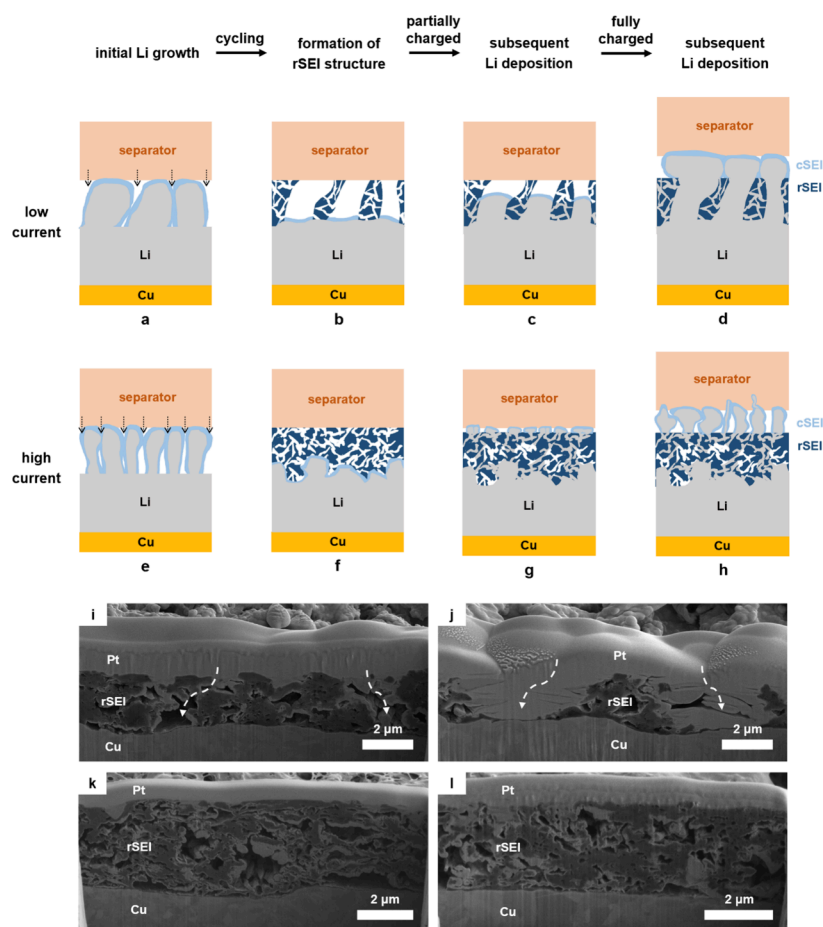
Figure 5. Schematic illustrations of rSEI structure formation and its impact on Li morphology under low (a−d) and high (e−h) current densities in weakly solvating fluoroether electrolytes. (a,e) Li electrode under a fully charged state in the initial cycle without rSEI. The arrows indicate areas with the most SEI accumulation. (b,f) Li electrode under a fully discharged state with rSEI (dark blue) after several cycles. (c,g) Li electrode under a partially charged state with rSEI. (d,h) Li electrode under fully charged state with rSEI. (i−l) FIB-SEM images of rSEI formed on the Cu electrode after 10 cycles (4 mAh cm^{-2}) at low (0.4 mA cm^{-2}, i,j) and high (4 mA cm^{-2}, k,l) plating current densities in the DEE-FDEB electrolyte. The cells were disassembled under fully stripped state. Pt was deposited before FIB sputtering to preserve the surface layer morphology. The dashed arrows in i and j indicate empty space directly connecting the top and bottom of rSEI. The scale bars are 2 μm.

observed for DEE-FDEB (the highest σ), while soft shorting occurred after about 30 cycles for DME-TTE (medium σ) and during the first charging step for FDMB (the lowest σ). A similar trend was observed at the C/2 charge rate. At even lower charge rates ($\leq$C/5), such a correlation was lost (Figure 3). These observations suggest that the failure modes for full cells are different at low and high charge rates. Therefore, electrolytes that lead to good cycle life at low charge rates may not be suitable for high charge rates. The higher Vincent−Bruce transport number (t_+) and effective Fickian diffusivity (D_{eff}) in FDMB were not sufficient to enable fast charging (Figure 3), likely limited by its poor ionic conductivity. Since the movement of ions is collectively determined by conductivity, diffusivity, and transference number,[28] the observations here suggest that it is important to simultaneously achieve high σ, D, and t_+ when designing electrolytes for fast charging.

Current-Density-Dependent Lithium and rSEI Morphology. To investigate the dependence of Li and rSEI morphology on plating current density, thin Li (50 μm thick) half-cells were constructed with a piece of thick Li as the counter electrode. All cells were activated at 0.4 mA cm^{-2} and 4 mAh cm^{-2} for two cycles, followed by 10 cycles at 0.4 or 4

mA cm^{-2} plating current densities to form the rSEI (low- or high-current formation). In the final step, 0.2, 0.5, or 1 mAh cm^{-2} capacity was plated at 4 mA cm^{-2} (high-current plating) or 0.4 mA cm^{-2} (low-current plating). These final plating capacities were less than 25% of the cycling capacity, which enabled the observation of initial Li growth by a scanning electron microscope (SEM). The current profiles are listed in Figure 4.

We first investigated Li and rSEI morphologies at low and high current densities in the DEE-FDEB electrolyte. Under the low-current formation and low-current plating conditions, large Li grains were observed in the 11th cycle and were separated by the rSEI (Figure 4a−c), similar to some previous observations.[10,41,46] Elemental mapping by energy-dispersive X-ray spectroscopy (EDS) confirmed the regions of Li and rSEI (Supplementary Figure S13), which are marked by yellow and green arrows, respectively, as shown in Figure 4b. The Li plating morphology observed here validated our previous hypothesis that in some weakly solvating fluoroether electrolytes, the plated Li first grew through the porous rSEI layer[46] before forming the typical pancake-like morphology[2,3,12] on the top of the rSEI. Under the slow-charging condition here, a minimum of 25% of cycled Li (1 out of 4 mAh cm^{-2}) was

surrounded by the rSEI as evidenced by the lack of Li plating above rSEI, as shown in Figure 4c.

Under the high-current formation and high-current plating conditions, a very different surface morphology was observed (Figure 4d−f). The regions of Li and rSEI were confirmed by EDS (Supplementary Figure S14). A more compact rSEI structure was formed (Figure 4d). At 0.2 mAh cm^{-2} deposition capacity, scarce and inhomogeneous Li nucleation was observed on the top of the rSEI (Figure 4d). As the deposition capacity increased, the Li grain size continued to increase (Figure 4d−f) but remained smaller than those as shown in Figure 4a−c. Importantly, unlike the morphology observed under the slow-charging condition, the plated Li was not surrounded by the rSEI after merely 0.2 mAh cm^{-2} capacity under the fast-charging condition. Since the SEI should be electrically insulating, there must be a small amount of Li growth within the rSEI (<0.2 mAh cm^{-2} or <5% of cycling capacity) connecting the uncycled Li underneath the rSEI and the plated Li above the rSEI. Such scarce and dispersed points for Li deposition led to significant inhomogeneity and hotspots for Li growth. The origin and effects of these morphologies will be discussed in the later sections.

The same sets of experiments were carried out for the DME-TTE electrolyte (Supplementary Figure S15a−f). The observations were identical to those described above. Furthermore, the zoomed-out SEM images for DEE-FDEB and DME-TTE samples (Supporting Information Figures S16, S17, S19, S20) are provided to show the generality of our observations. Additional experiments under high-current formation and low-current plating were carried out to investigate the relative contributions from current density and rSEI structure to Li morphology (Figure 4g−i, S15g−i, S18, and S21). Details will be discussed in later sections.

Formation of rSEI Structure and Its Impact on Li Morphology. In addition to the compact SEI (cSEI, the film in direct contact with Li metal),[1,47] our groups previously discovered the unconventional rSEI structure in the FDMB electrolyte in anode-free Cu‖LFP cells (2.2 mAh cm^{-2}) after around 100 cycles at C/5.[46] The cross-sectional images revealed that the rSEI was sandwiched between the Cu current collector and deposited Li. Therefore, during charging, Li grew from the Cu current collector upward through the porous rSEI structure before finally depositing as large grains on the top of the rSEI. It was proposed that the interfacial energy, surface Li diffusivity, and structural support of the rSEI derived from FSI$^-$ are critical for the improved Li stability in the FDMB electrolyte.[46] A similar porous rSEI structure was also reported for the DME-TTE electrolyte.[6] Notably, the growth of Li within and on the top of the rSEI appears to be unique to weakly solvating fluoroether electrolytes, whereas Li deposition underneath the rSEI was more commonly observed in carbonate electrolytes (as illustrated in Supplementary Figure S22).[22,23,48]

Since the rSEI is formed by the accumulation of cSEI and dead Li throughout cycling,[6,46] we hypothesize that the structure of rSEI is modulated by Li morphology in the initial cycles through the following processes. (1) The deposited Li grains with higher surface/volume ratios have more cSEI, thereby leading to more rSEI accumulation. (2) Most rSEI accumulates from the cSEI on the side of Li grains as the Li shrinks and the cSEI folds during discharging (as indicated by arrows in Figure 5a,e). In comparison, the rSEI from the cSEI on the flat top surface of Li is thinner. It might break more

easily and move to the side of expanding Li grains during charging. (3) Bulky Li grains create larger voids within the rSEI, whereas mossy Li creates more compact rSEI.

Given the large exchange current densities in the fluoroether electrolytes (Supporting Information Table S2), we hypothesize that the Li plating is mass transfer-controlled. The faster mass transfer toward the tips of an uneven Li surface leads to poor deposition morphology, and this process can be accelerated by high current density and slow ion transport in electrolytes.[49−51] Consequently, under the fast-charging condition, the plated Li has a high surface/volume ratio, which leads to more rSEI in tightly packed structures (Figure 5f). In contrast, since the slow-charging condition favors bulky Li deposition, less rSEI is formed and is separated by large voids (Figure 5b). These hypotheses are consistent with our observation of large Li grains separated by the porous rSEI at low current densities and small Li grains on the top of a compact rSEI at high current densities (Figure 4).

We characterized the cross sections of the rSEI by SEM. A Cu electrode was used instead of thin Li to show better contrast between the rSEI and the substrate. The rSEI was formed by cycling Li‖Cu half-cells in the DEE-FDEB electrolyte at either 0.4 mA cm^{-2} (low current) or 4 mA cm^{-2} (high current) plating current density for 10 cycles. The cells were disassembled under the stripped state, and cross sections were prepared by a focused ion beam (FIB). The rSEI formed under high current showed closely packed structures (Figure 5k,l). The pores appeared to be tortuous since no direct pathway between the bottom and the top of the rSEI could be observed on the 2D cross section. In contrast, the rSEI formed under low current was thinner and showed channels connecting the top and the bottom of the rSEI (Figure 5i). We also observed patches of the rSEI separated by empty volume (Figures 5j and S23), which was presumably occupied by Li in the plated state. These observations were consistent with our hypothesis above. In addition, the rSEI thickened with cycling, as evidenced by comparing the electrodes cycled at 4 mA cm^{-2} for 10 and 30 cycles (Figures 5k,l and S24). The exact progression of the rSEI over cycling requires further investigations.

We further hypothesize that the structure of the rSEI could modulate the subsequent Li morphology. Under the low-current condition, the rSEI is inhomogeneous with large voids for subsequent Li growth (Figure 5b,i,j). We observed Li deposition in large grains to fill the voids (Figures 5c, 4a−c, and S15a−c) before growing uniformly on the top of the rSEI (Figure 5d). Notably, a minimum of 25% of the cycled Li was plated within the rSEI structure as estimated in the previous sections, highlighting the important role of the rSEI in modulating Li plating under low current densities. Under the high-current conditions, we observed a more compact rSEI (Figure 5f,k,l). The small voids within the rSEI likely guide high-aspect-ratio Li deposition morphology through the rSEI (Figure 5g). In addition, the high current density should favor the upward growth of Li. As a result, only a small amount of Li is plated within the rSEI (Figure 5g), after which most new Li deposition occurs above the rSEI (Figure 5h). This was evidenced by the small Li grains on the top of the rSEI after plating only 0.2 mAh cm^{-2} capacity (Figures 4d and S15d). In this case, the rSEI creates an inhomogeneous electrode surface where the electrochemically active area is limited and dispersed, which further increases the local current density. The repeated formation of a large amount of high-surface-area

Li above the rSEI will eventually penetrate the separator and lead to soft shorting.

As a control experiment, we formed rSEI at 4 mA cm^{-2}, followed by plating Li at 0.4 mA cm^{-2} (high-current formation and low-current plating) (Figures 4g–i, S15g–i, S18, and S21). We again focus our discussions on the DEE-FDEB electrolyte first. Compared to Figure 4d−f (high-current formation and high-current plating), the amount of Li plated within the rSEI was higher, as shown in Figure 4g–i, as evidenced by the lower coverage of Li on the top of the rSEI. In addition, the Li grain size was larger, as shown in Figure 4g−i. These differences validated that the upward anisotropic growth of Li is favored under higher current densities even in the presence of the same rSEI. Compared to the Li morphology, as shown in Figure 4a−c (low-current formation and low-current plating), the plated Li was less homogeneous and grew well above the rSEI, as shown in Figure 4g−i. Therefore, the rSEI structure formed under high current densities can indeed guide undesirable Li deposition morphology even after switching to lower plating current densities. This leads to the inhomogeneous electrochemically active surface for further Li deposition above the rSEI. The same sets of experiments were carried out for the DME-TTE electrolyte. The general trend was similar to what was observed in the DEE-FDEB electrolyte albeit slight differences (Supplementary Figures S15g−i, S21, and notes).

Other Factors Considered for Fast-Charging Stability. We further consider other factors that might limit the fast-charging stability of LMBs using the fluoroether electrolytes. The details are provided in Supplementary Figures S25−S34 and notes. (1) Increasing the Li metal thickness or the electrolyte volume did not impact cycle life, indicating that the cycle life at 1C was not limited by Li inventory or electrolyte depletion.[6,48] (2) The reconstructed cell using the 1C cycled NMC showed complete capacity recovery, proving that the cell capacity decay was not due to NMC degradation. (3) Various Li‖Li cell tests showed the short-circuit behavior distinctive from Sand's time,[49] indicating that complete surface ion depletion is not a requirement for the internal short circuit. (4) The galvanostatic staircase measurements found no evidence of complete SEI breakdown in the fluoroether electrolytes, which is quite different from the carbonate electrolytes and which likely reflects the robustness of the SEI.[30] (5) Measured by EIS in Li‖Li cells, the electrolyte resistance dominates over SEI resistance, demonstrating the need to further improve bulk ion transport. In summary, the fast-charging stability was not limited by these factors. Therefore, we can attribute the internal short circuit during fast charging to the current-dependent interplay between the Li deposition morphology and the rSEI morphology.

CONCLUSIONS

Many promising electrolyte designs have been reported to enable stable cycling of LMBs under slow-charging conditions. However, since the development of LMBs is largely motivated by their application in the transportation sector, fast-charging capability is an important requirement. In this work, we evaluated three weakly solvating fluoroether electrolytes that enabled stable cycling at low charge rates. However, all of them showed soft shorting behavior when cycled at high charge rates, which was attributed to the current-dependent interplay between the Li deposition morphology and the rSEI morphology. The structure of the rSEI is modulated by Li plating morphology in the initial cycles. Subsequently, the rSEI guides the deposition morphology of Li. In the fluoroether electrolytes, the rSEI structure formed under a lower current density allows bulky Li deposition, whereas that formed under a higher current density aggravates the inhomogeneous and anisotropic growth of Li.

Additionally, the stability of LMBs under higher charge current densities seemed to have a correlation with ion transport properties—an aspect that requires further understanding. The design of weakly solvating electrolytes must overcome a paradox: increased Li$^+$-FSI$^-$ ion pairs and aggregates can improve CE but may slow ion transport. Therefore, proper characterization and understanding of ion transport properties are crucial for the future electrolytes.[52] Encouragingly, a recent report demonstrated fast-charging LMBs under stringent conditions by electrolyte design with high ionic conductivity,[53] showing significant room for improvement in this field.

ASSOCIATED CONTENT

Supporting Information

The Supporting Information is available free of charge at https://pubs.acs.org/doi/10.1021/acs.jpcc.4c01740.

Comparison of electrolyte performance from the recent literature; design and characterization of DEE-FDEB electrolyte; additional electrochemical characterizations; additional SEM images and EDS maps; and synthesis and NMR spectra (PDF)

AUTHOR INFORMATION

Corresponding Authors

Yi Cui − Department of Materials Science and Engineering, Stanford University, Stanford, California 94305, United States; Stanford Institute for Materials and Energy Sciences, SLAC National Accelerator Laboratory, Menlo Park, California 94025, United States; orcid.org/0000-0002-6103-6352; Email: yicui@stanford.edu

Zhenan Bao − Department of Chemical Engineering, Stanford University, Stanford, California 94305, United States; orcid.org/0000-0002-0972-1715; Email: zbao@stanford.edu

Authors

Yuelang Chen − Department of Chemical Engineering and Department of Chemistry, Stanford University, Stanford, California 94305, United States; orcid.org/0000-0002-5249-0596

Zhiao Yu − Department of Chemical Engineering and Department of Chemistry, Stanford University, Stanford, California 94305, United States; orcid.org/0000-0001-8746-1640

Huaxin Gong − Department of Chemical Engineering, Stanford University, Stanford, California 94305, United States; orcid.org/0000-0002-2493-0793

Wenbo Zhang − Department of Materials Science and Engineering, Stanford University, Stanford, California 94305, United States; orcid.org/0000-0002-0828-594X

Paul Rudnicki − Department of Chemical Engineering, Stanford University, Stanford, California 94305, United States; orcid.org/0000-0003-3518-1721

Zhuojun Huang − Department of Materials Science and Engineering, Stanford University, Stanford, California 94305, United States; orcid.org/0000-0001-6236-8693

Weilai Yu − *Department of Chemical Engineering, Stanford University, Stanford, California 94305, United States;* orcid.org/0000-0002-9420-0702

Sang Cheol Kim − *Department of Materials Science and Engineering, Stanford University, Stanford, California 94305, United States;* orcid.org/0000-0002-1749-8277

David T. Boyle − *Department of Chemistry and Department of Materials Science and Engineering, Stanford University, Stanford, California 94305, United States;* orcid.org/0000-0002-0452-275X

Philaphon Sayavong − *Department of Chemistry and Department of Materials Science and Engineering, Stanford University, Stanford, California 94305, United States;* orcid.org/0000-0001-7605-8194

Hasan Celik − *College of Chemistry Nuclear Magnetic Resonance Facility (CoC-NMR), University of California, Berkeley, California 94720, United States*

Rong Xu − *Department of Materials Science and Engineering, Stanford University, Stanford, California 94305, United States;* orcid.org/0000-0002-3694-595X

Yangju Lin − *Department of Chemical Engineering, Stanford University, Stanford, California 94305, United States;* orcid.org/0000-0001-6378-7179

Shaoyang Wang − *Department of Chemical Engineering, Stanford University, Stanford, California 94305, United States*

Jian Qin − *Department of Chemical Engineering, Stanford University, Stanford, California 94305, United States;* orcid.org/0000-0001-6271-068X

Complete contact information is available at:
https://pubs.acs.org/10.1021/acs.jpcc.4c01740

Notes

■ ACKNOWLEDGMENTS

■ REFERENCES

(1) Wang, H.; Yu, Z.; Kong, X.; Kim, S. C.; Boyle, D. T.; Qin, J.; Bao, Z.; Cui, Y. Liquid Electrolyte: The Nexus of Practical Lithium Metal Batteries. *Joule* **2022**, *6* (3), 588−616.

(2) Yu, Z.; Wang, H.; Kong, X.; Huang, W.; Tsao, Y.; Mackanic, D. G.; Wang, K.; Wang, X.; Huang, W.; Choudhury, S.; et al. Molecular Design for Electrolyte Solvents Enabling Energy-Dense and Long-Cycling Lithium Metal Batteries. *Nat. Energy* **2020**, *5* (7), 526−533.

(3) Ren, X.; Zou, L.; Cao, X.; Engelhard, M. H.; Liu, W.; Burton, S. D.; Lee, H.; Niu, C.; Matthews, B. E.; Zhu, Z.; et al. Enabling High-Voltage Lithium-Metal Batteries under Practical Conditions. *Joule* **2019**, *3* (7), 1662−1676.

(4) Liu, H.; Holoubek, J.; Zhou, H.; Chen, A.; Chang, N.; Wu, Z.; Yu, S.; Yan, Q.; Xing, X.; Li, Y.; et al. Ultrahigh Coulombic Efficiency Electrolyte Enables Li∥SPAN Batteries with Superior Cycling Performance. *Mater. Today* **2021**, *42* (xx), 17−28.

(5) Yoo, D.; Yang, S.; Kim, K. J.; Choi, J. W. Fluorinated Aromatic Diluent for High-Performance Lithium Metal Batteries. *Angew. Chem.* **2020**, *132* (35), 14979−14986.

(6) Niu, C.; Liu, D.; Lochala, J. A.; Anderson, C. S.; Cao, X.; Gross, M. E.; Xu, W.; Zhang, J. G.; Whittingham, M. S.; Xiao, J.; et al. Balancing Interfacial Reactions to Achieve Long Cycle Life in High-Energy Lithium Metal Batteries. *Nat. Energy* **2021**, *6* (7), 723−732.

(7) Zhang, H.; Zeng, Z.; He, R.; Wu, Y.; Hu, W.; Lei, S.; Liu, M.; Cheng, S.; Xie, J. 1,3,5-Trifluorobenzene and Fluorobenzene Co-Assisted Electrolyte with Thermodynamic and Interfacial Stabilities for High-Voltage Lithium Metal Battery. *Energy Storage Mater.* **2022**, *48*, 393−402.

(8) Eldesoky, A.; Louli, A. J.; Benson, A.; Dahn, J. R. Cycling Performance of NMC811 Anode-Free Pouch Cells with 65 Different Electrolyte Formulations. *J. Electrochem. Soc.* **2021**, *168* (12), 120508.

(9) Weber, R.; Genovese, M.; Louli, A. J.; Hames, S.; Martin, C.; Hill, I. G.; Dahn, J. R. Long Cycle Life and Dendrite-Free Lithium Morphology in Anode-Free Lithium Pouch Cells Enabled by a Dual-Salt Liquid Electrolyte. *Nat. Energy* **2019**, *4* (8), 683−689.

(10) Louli, A. J.; Eldesoky, A.; Weber, R.; Genovese, M.; Coon, M.; deGooyer, J.; Deng, Z.; White, R. T.; Lee, J.; Rodgers, T.; et al. Diagnosing and Correcting Anode-Free Cell Failure via Electrolyte and Morphological Analysis. *Nat. Energy* **2020**, *5* (9), 693−702.

(11) Kim, M. S.; Zhang, Z.; Rudnicki, P. E.; Yu, Z.; Wang, J.; Wang, H.; Oyakhire, S. T.; Chen, Y.; Kim, S. C.; Zhang, W.; et al. Suspension Electrolyte with Modified Li+ Solvation Environment for Lithium Metal Batteries. *Nat. Mater.* **2022**, *21*, 445−454.

(12) Yu, Z.; Rudnicki, P. E.; Zhang, Z.; Huang, Z.; Celik, H.; Oyakhire, S. T.; Chen, Y.; Kong, X.; Kim, S. C.; Xiao, X.; et al. Rational Solvent Molecule Tuning for High-Performance Lithium Metal Battery Electrolytes. *Nat. Energy* **2022**, *7* (1), 94−106.

(13) Holoubek, J.; Liu, H.; Wu, Z.; Yin, Y.; Xing, X.; Cai, G.; Yu, S.; Zhou, H.; Pascal, T. A.; Chen, Z.; et al. Tailoring Electrolyte Solvation for Li Metal Batteries Cycled at Ultra-Low Temperature. *Nat. Energy* **2021**, *6*, 303−313.

(14) Xue, W.; Huang, M.; Li, Y.; Zhu, Y. G.; Gao, R.; Xiao, X.; Zhang, W.; Li, S.; Xu, G.; Yu, Y.; et al. Ultra-High-Voltage Ni-Rich Layered Cathodes in Practical Li Metal Batteries Enabled by a Sulfonamide-Based Electrolyte. *Nat. Energy* **2021**, *6*, 495−505.

(15) Fan, X.; Chen, L.; Borodin, O.; Ji, X.; Chen, J.; Hou, S.; Deng, T.; Zheng, J.; Yang, C.; Liou, S. C.; et al. Non-Flammable Electrolyte Enables Li-Metal Batteries with Aggressive Cathode Chemistries. *Nat. Nanotechnol.* **2018**, *13* (8), 715.

(16) Chen, Y.; Yu, Z.; Rudnicki, P.; Gong, H.; Huang, Z.; Kim, S. C.; Lai, J.-C.; Kong, X.; Qin, J.; Cui, Y.; et al. Steric Effect Tuned Ion Solvation Enabling Stable Cycling of High-Voltage Lithium Metal Battery. *J. Am. Chem. Soc.* **2021**, *143* (44), 18703−18713.

(17) Qian, J.; Henderson, W. A.; Xu, W.; Bhattacharya, P.; Engelhard, M.; Borodin, O.; Zhang, J. G. High Rate and Stable Cycling of Lithium Metal Anode. *Nat. Commun.* **2015**, *6*, 6362.

(18) Lee, M. S.; Roev, V.; Jung, C.; Kim, J. R.; Han, S.; Kang, H. R.; Im, D.; Kim, I. S. An Aggregate Cluster-Dispersed Electrolyte Guides the Uniform Nucleation and Growth of Lithium at Lithium Metal Anodes. *ChemistrySelect* **2018**, *3* (41), 11527−11534.

(19) Huang, F.; Ma, G.; Wen, Z.; Jin, J.; Xu, S.; Zhang, J. Enhancing Metallic Lithium Battery Performance by Tuning the Electrolyte Solution Structure. *J. Mater. Chem. A* **2018**, *6* (4), 1612−1620.

(20) Logan, E. R.; Dahn, J. R. Electrolyte Design for Fast-Charging Li-Ion Batteries. *Trends Chem.* **2020**, *2*, 354−366.

(21) Zheng, J.; Engelhard, M. H.; Mei, D.; Jiao, S.; Polzin, B. J.; Zhang, J. G.; Xu, W. Electrolyte Additive Enabled Fast Charging and Stable Cycling Lithium Metal Batteries. *Nat. Energy* **2017**, *2* (3), 17012.

(22) Lv, D.; Shao, Y.; Lozano, T.; Bennett, W. D.; Graff, G. L.; Polzin, B.; Zhang, J.; Engelhard, M. H.; Saenz, N. T.; Henderson, W. A.; et al. Failure Mechanism for Fast-Charged Lithium Metal Batteries

with Liquid Electrolytes. *Adv. Energy Mater.* **2015**, *5* (3), No. 1400993.

(23) Jiao, S.; Zheng, J.; Li, Q.; Li, X.; Engelhard, M. H.; Cao, R.; Zhang, J. G.; Xu, W. Behavior of Lithium Metal Anodes under Various Capacity Utilization and High Current Density in Lithium Metal Batteries. *Joule* **2018**, *2* (1), 110−124.

(24) Adams, B. D.; Zheng, J.; Ren, X.; Xu, W.; Zhang, J. G. Accurate Determination of Coulombic Efficiency for Lithium Metal Anodes and Lithium Metal Batteries. *Adv. Energy Mater.* **2018**, *8* (7), 1−11.

(25) Kim, S. C.; Kong, X.; Vilá, R. A.; Huang, W.; Chen, Y.; Boyle, D. T.; Yu, Z.; Wang, H.; Bao, Z.; Qin, J.; et al. Potentiometric Measurement to Probe Solvation Energy and Its Correlation to Lithium Battery Cyclability. *J. Am. Chem. Soc.* **2021**, *143* (27), 10301−10308.

(26) Thompson, S. D.; Newman, J. Differential Diffusion Coefficients of Sodium Polysulfide Melts. *J. Electrochem. Soc.* **1989**, *136* (11), 3362−3369.

(27) Wang, A. A.; Hou, T.; Karanjavala, M.; Monroe, C. W. Shifting-Reference Concentration Cells to Refine Composition-Dependent Transport Characterization of Binary Lithium-Ion Electrolytes. *Electrochim. Acta* **2020**, *358*, No. 136668.

(28) Wang, A. A.; Gunnarsdóttir, A. B.; Fawdon, J.; Pasta, M.; Grey, C. P.; Monroe, C. W. Potentiometric MRI of a Superconcentrated Lithium Electrolyte: Testing the Irreversible Thermodynamics Approach. *ACS Energy Lett.* **2021**, *6* (9), 3086−3095.

(29) Boyle, D. T.; Kong, X.; Pei, A.; Rudnicki, P. E.; Shi, F.; Huang, W.; Bao, Z.; Qin, J.; Cui, Y. Transient Voltammetry with Ultramicroelectrodes Reveals the Electron Transfer Kinetics of Lithium Metal Anodes. *ACS Energy Lett.* **2020**, *5* (3), 701−709.

(30) Boyle, D. T.; Li, Y.; Pei, A.; Vilá, R. A.; Zhang, Z.; Sayavong, P.; Kim, M. S.; Huang, W.; Wang, H.; Liu, Y.; et al. Resolving Current-Dependent Regimes of Electroplating Mechanisms for Fast Charging Lithium Metal Anodes. *Nano Lett.* **2022**, *22* (20), 8224−8232.

(31) Su, C. C.; He, M.; Amine, R.; Rojas, T.; Cheng, L.; Ngo, A. T.; Amine, K. Solvating Power Series of Electrolyte Solvents for Lithium Batteries. *Energy Environ. Sci.* **2019**, *12* (4), 1249−1254.

(32) Abraham, M. J.; Murtola, T.; Schulz, R.; Páll, S.; Smith, J. C.; Hess, B.; Lindah, E. Gromacs: High Performance Molecular Simulations through Multi-Level Parallelism from Laptops to Supercomputers. *SoftwareX* **2015**, *1−2*, 19−25.

(33) Jorgensen, W. L.; Maxwell, D. S.; Tirado-Rives, J. Development and Testing of the OPLS All-Atom Force Field on Conformational Energetics and Properties of Organic Liquids. *J. Am. Chem. Soc.* **1996**, *118* (45), 11225−11236.

(34) Dodda, L. S.; De Vaca, I. C.; Tirado-Rives, J.; Jorgensen, W. L. LigParGen Web Server: An Automatic OPLS-AA Parameter Generator for Organic Ligands. *Nucleic Acids Res.* **2017**, *45* (W1), W331−W336.

(35) Frisch, M. J.; Trucks, G. W.; Schlegel, H. B.; Scuseria, G. E.; Robb, M. A.; Cheeseman, J. R.; Scalmani, G.; Barone, V.; Petersson, G. A.; Nakatsuji, H.; et al. *Gaussian 16, Revision B.01*. Gaussian Inc.: Wallingford CT, 2016.

(36) Leontyev, I.; Stuchebrukhov, A. Accounting for Electronic Polarization in Non-Polarizable Force Fields. *Phys. Chem. Chem. Phys.* **2011**, *13* (7), 2613−2626.

(37) Self, J.; Fong, K. D.; Persson, K. A. Transport in Super-concentrated LiPF6 and LiBF4/Propylene Carbonate Electrolytes. *ACS Energy Lett.* **2019**, *4* (12), 2843−2849.

(38) Michaud-Agrawal, N.; Denning, E. J.; Woolf, T. B.; Beckstein, O. Software News and Updates MDAnalysis: A Toolkit for the Analysis of Molecular Dynamics Simulations. *J. Comput. Chem.* **2011**, *32* (10), 2319−2327.

(39) Qian, J.; Adams, B. D.; Zheng, J.; Xu, W.; Henderson, W. A.; Wang, J.; Bowden, M. E.; Xu, S.; Hu, J.; Zhang, J. G. Anode-Free Rechargeable Lithium Metal Batteries. *Adv. Funct. Mater.* **2016**, *26* (39), 7094−7102.

(40) Zheng, J.; Yan, P.; Mei, D. H.; Engelhard, M. H.; Cartmell, S. S.; Polzin, B. J.; Wang, C. M.; Zhang, J. G.; Xu, W. Highly Stable Operation of Lithium Metal Batteries Enabled by the Formation of a Transient High-Concentration Electrolyte Layer. *Adv. Energy Mater.* **2016**, *6* (8), 1−10.

(41) Louli, A. J.; Coon, M.; Genovese, M.; deGooyer, J.; Eldesoky, A.; Dahn, J. R. Optimizing Cycling Conditions for Anode-Free Lithium Metal Cells. *J. Electrochem. Soc.* **2021**, *168* (2), No. 020515.

(42) Xu, K. Navigating the Minefield of Battery Literature. *Commun. Mater.* **2022**, *3* (1), 1−7.

(43) Dollé, M.; Sannier, L.; Beaudoin, B.; Trentin, M.; Tarascon, J. M. Live Scanning Electron Microscope Observations of Dendritic Growth in Lithium/Polymer Cells. *Electrochem. Solid-State Lett.* **2002**, *5* (12), A286−A289.

(44) Kong, L.; Xing, Y.; Pecht, M. G. In-Situ Observations of Lithium Dendrite Growth. *IEEE Access* **2018**, *6*, 8387−8393.

(45) Liu, F.; Xu, R.; Wu, Y.; Boyle, D. T.; Yang, A.; Xu, J.; Zhu, Y.; Ye, Y.; Yu, Z.; Zhang, Z.; et al. Dynamic Spatial Progression of Isolated Lithium during Battery Operations. *Nature* **2021**, *600* (7890), 659−663.

(46) Wang, H.; Huang, W.; Yu, Z.; Huang, W.; Xu, R.; Zhang, Z.; Bao, Z.; Cui, Y. Efficient Lithium Metal Cycling over a Wide Range of Pressures from an Anion-Derived Solid-Electrolyte Interphase Framework. *ACS Energy Lett.* **2021**, *6*, 816−825.

(47) Zhang, J. G.; Xu, W.; Xiao, J.; Cao, X.; Liu, J. Lithium Metal Anodes with Nonaqueous Electrolytes. *Chem. Rev.* **2020**, *120* (24), 13312−13348.

(48) Jo, Y.; Jin, D.; Lim, M.; Lee, H.; An, H.; Seo, J.; Kim, G.; Ren, X.; Lee, Y. M.; Lee, H. Structural and Chemical Evolutions of Li/Electrolyte Interfaces in Li-Metal Batteries: Tracing Compositional Changes of Electrolytes under Practical Conditions. *Adv. Sci. (Weinheim, Ger.)* **2023**, *10*, No. e2204812.

(49) Wu, Z.; Liu, H.; Holoubek, J.; Anderson, C.; Shi, L.; Khemchandani, H.; Lu, D.; Liu, D.; Niu, C.; Xiao, J.; et al. The Role of Ion Transport in the Failure of High Areal Capacity Li Metal Batteries. *ACS Energy Lett.* **2022**, *7*, 2701−2710.

(50) Monroe, C.; Newman, J. Dendrite Growth in Lithium/Polymer Systems. *J. Electrochem. Soc.* **2003**, *150* (10), A1377.

(51) Xu, X.; Jiao, X.; Kapitanova, O. O.; Wang, J.; Volkov, V. S.; Liu, Y.; Xiong, S. Diffusion Limited Current Density: A Watershed in Electrodeposition of Lithium Metal Anode. *Adv. Energy Mater.* **2022**, *12* (19), No. 2200244.

(52) Fong, K. D.; Self, J.; McCloskey, B. D.; Persson, K. A. Ion Correlations and Their Impact on Transport in Polymer-Based Electrolytes. *Macromolecules* **2021**, *54* (6), 2575−2591.

(53) Zhang, W.; Lu, Y.; Wan, L.; Zhou, P.; Xia, Y.; Yan, S.; Chen, X.; Zhou, H.; Dong, H.; Liu, K. Engineering a Passivating Electric Double Layer for High Performance Lithium Metal Batteries. *Nat. Commun.* **2022**, *13* (1), 2029.